Strain fluctuations unlock ferroelectricity in wurtzites

Steven M. Baksa[1], Simon Gelin[1], Seda Oturak[1], Robert Jackson Spurling[1], Alireza Sepehrinezhad[2], Leonard Jacques[1], Susan E. Trolier-McKinstry[1], Adri C. T. van Duin[3], Jon-Paul Maria[1], Andrew M. Rappe[4], and Ismaila Dabo[1]

[1]Department of Materials Science and Engineering, Pennsylvania State University, University Park, Pennsylvania, United States, 16802
[2]Department of Engineering Science and Mechanics, Pennsylvania State University, University Park, Pennsylvania, United States, 16802
[3]Department of Mechanical Engineering, Pennsylvania State University, University Park, Pennsylvania, United States, 16802
[4]Department of Chemistry, University of Pennsylvania, Philadelphia, Pennsylvania, United States, 19104

Abstract

Ferroelectrics are of practical interest for non-volatile data storage due to their reorientable, crystallographically defined polarization. Yet efforts to integrate conventional ferroelectrics into ultrathin memories have been frustrated by film-thickness limitations, which impede polarization reversal under low voltage. Wurtzite materials, including magnesium-substituted zinc oxide (Zn,Mg)O, have been shown to exhibit scalable ferroelectricity as thin films. In this work, we explain the origins of ferroelectricity in (Zn,Mg)O. Large strain fluctuations emerge locally in (Zn,Mg)O, causing a reduction of up to 45% in the local coercive field. We provide concurrent experimental and computational evidence of these effects by demonstrating polarization switching in ZnO–(Zn,Mg)O heterostructures. This work opens up an avenue to develop scalable ferroelectrics by controlling local strain gradients.

Keywords: Ferroelectrics, thin films, device scaling, microelectronics, random-access memories

1 Introduction

Ferroelectric thin films can reverse their crystallographically defined polarization states under low electric bias, making them attractive candidates for storing binary data in energy-efficient (low-voltage) microelectronics [1, 2]. Cation substitution is an effective approach for promoting polarization reversal in prototypical ferroelectrics like titanate-based perovskite oxides [3, 4]. For instance, $Pb(Zr,Ti)O_3$ (Zr-substituted $PbTiO_3$) exhibits enhanced polarizability relative to its $PbTiO_3$ and $PbZrO_3$ end members [5] due to competing polar structures at the morphotropic (tetragonal-to-rhombohedral) phase boundary. This phase instability leads to a high dielectric constant, making it an appealing ferroelectric.

While $Pb(Zr,Ti)O_3$ has been successfully integrated into random-access ferroelectric memories [6], there exist scaling constraints for film thicknesses below 70 nm, which limit the ferroelectric

performance and energy efficiency of $Pb(Zr,Ti)O_3$-based thin-film microelectronics [7, 8, 9, 10, 11]. As an alternative to perovskite materials, fluorites [12, 13, 14], including hafnia (HfO_2) and its derivatives (for example, $(Hf,La)O_2$, $(Hf,Zr)O_2$, and $(Hf,Gd)O_2$) [15, 16, 17, 18], have been shown to be scalable down to 2 nm [16, 17, 18, 19, 20, 21, 22, 23, 24]. Although endurance of up to 10^{10} cycles have been reported [15, 16, 20], ferroelectricity in hafnia is typically optimized at synthesis temperatures above 800 °C to reduce wake up from a pristine to cycled state, whereas back-end-of-the-line processing necessitates deposition temperatures below 400 °C. Studies into $(Hf,Zr)O_2$ thin films at low annealing temperatures (<400 ° C) show ferroelectric responses with a remanent polarization of 23.5 μC cm^{-2} and coercive voltage of 1.25 V [19, 25].

Unlike perovskites and fluorites, wurtzites [14, 26, 27, 28, 29] can be synthesized under nominal processing conditions and exhibit a stable polar phase with no observable Curie temperature below their melting point [30]. Although wurtzites tend to have significant polarization reversal barriers, a dopant atom can stress the polar structure to the point of inducing a ferroelectric response at low bias, as is the case for (Al,Sc)N, which exhibits a remanent polarization of 80 μC cm^{-2} with a coercive field of 3.1 MV cm^{-1} [31, 32, 33, 34]. Similarly, while ZnO adopts a polar wurtzite structure that is generally not considered to be ferroelectric due to its high coercive field (>7 MV cm^{-1}) [26], it has been shown experimentally that (Zn,Mg)O, in less than forty cycles [**?**], is a ferroelectric material with a remanent polarization over 100 μC cm^{-2} and a coercive field as low as 2.7 MV cm^{-1} [35], although the underlying mechanisms of this induced ferroelectricity remain elusive.

It has been proposed that epitaxial strain can impart ferroelectricity to polar materials like wurtzite ZnO (Figure 1) [26, 27, 28, 31]. For instance, a biaxial tension orthogonal to the polar axis of 1.5% can reduce the reversal barrier by 20%. First-principles studies have suggested that a uniaxial compression of 6.0 GPa along the [0001] direction stabilizes an intermediate hexagonal phase in ZnO [36]. Using this insight, strain induced by Mg dopants was considered as a possible mechanism for ferroelectric reversal in (Zn,Mg)O; however, the magnitude of this biaxial strain is below 0.3%, which cannot explain such a large change in the ferroelectric switching barriers.

In this work, this discrepancy is resolved by showing that local strain fluctuations can unlock ferroelectric switching in (Zn,Mg)O. The possibility to promote ferroelectricity *via* local strain gradients offers a versatile strategy to develop and process low-temperature scalable ferroelectric thin films and heterostructures for microelectronic memories and switches.

2 Results and discussion

2.1 Influence of cation substitution on strain fluctuations

The formation of (Zn,Mg)O is critically dependent on the solubility of Mg cations in ZnO. To predict this solubility, the mixing enthalpy of (Zn,Mg)O as a function of Mg content for the end-member (wurtzite and rocksalt) phases was calculated as $\Delta H_{\text{mix}}(x) = H_{\text{Zn}_{1-x}\text{Mg}_x\text{O}} - (1-x)H_{\text{ZnO}} - xH_{\text{MgO}}$, where x is the Mg fraction as a decimal, $H_{\text{Zn}_{1-x}\text{Mg}_x\text{O}}$ is the energy of the (Zn,Mg)O configuration per formula unit, and H_{ZnO} and H_{MgO} are the reference enthalpies of ZnO and MgO, respectively. The results of these calculations, shown in Figure 2(a) and (b), indicate that mixing is favored across the full composition range for the wurtzite and rocksalt structures. Yet the shallow depths of –17.5 and –20 meV per formula unit (comparable to the thermal energy under processing conditions) for the wurtzite and rocksalt phases, respectively, and the existence of multiple configurations near the convex hull suggest that thermal disorder may impact local structural motifs in (Zn,Mg)O.

To include thermal effects, a cluster expansion model [42, 43, 44] was constructed and Wang–Landau sampling [45, 46, 47] was applied to predict the temperature-dependent Gibbs free energies

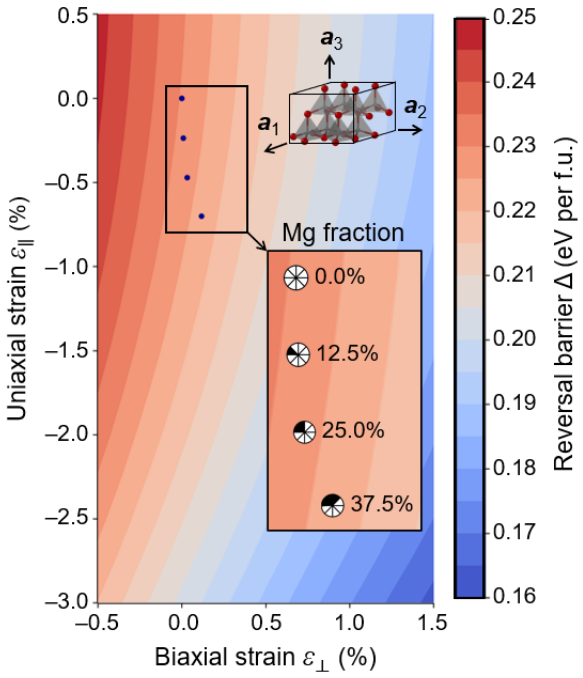

Figure 1: Polarization reversal barriers as a function of biaxial tension $\varepsilon_{\perp}$ and uniaxial compression $\varepsilon_{\parallel}$ (orthogonal and parallel to the polar axis, respectively; as shown in the inset) calculated from first principles. Lattice strains $\varepsilon_{\perp}$ and $\varepsilon_{\parallel}$ associated with the lowest-energy, fully relaxed (Zn,Mg)O geometries relative to bulk ZnO up to the solubility limit of Mg (ca. 40%) are also shown as points.

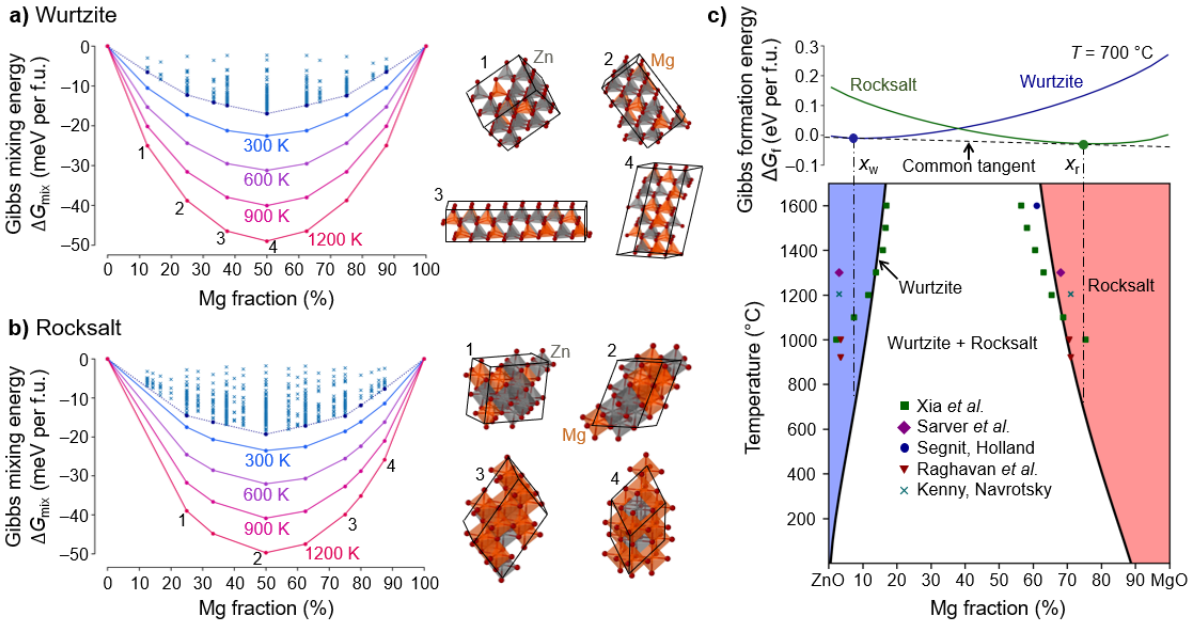

Figure 2: Convex hulls and representative structures at finite temperature of the (a) wurtzite and (b) rocksalt phases computed from density-functional theory. (c) Calculated phase diagram of the ZnO:MgO binary constructed from cluster expansions and Monte Carlo simulations *via* Wang-Landau sampling. The Gibbs free formation energies, ΔG_{f}, of each phase were employed to calculate the phase boundaries, x_{w} and x_{r}, as a function of temperature. Computed phase boundaries and experimental data (Refs. [37, 38, 39, 40, 41]) are indicated with solid lines and points, respectively.

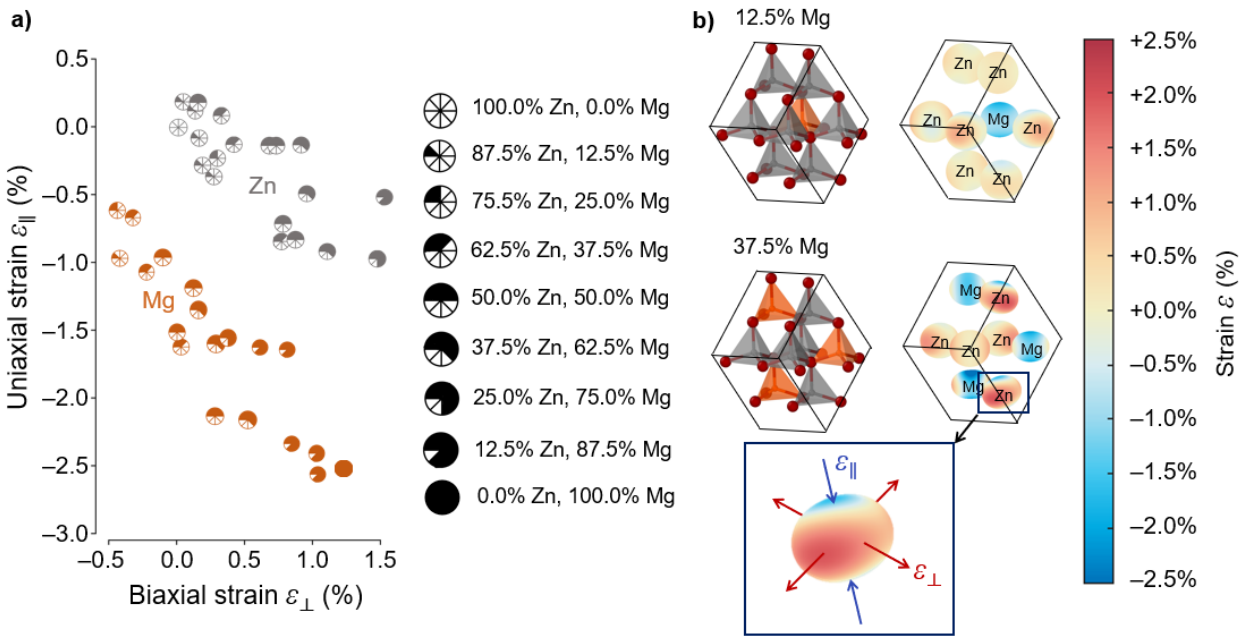

Figure 3: (a) Calculated strains of the Zn (grey) and Mg (orange) cations as a function of Mg fraction. The Zn cations have a mixture of $\varepsilon_\perp$ and $\varepsilon_\parallel$, whereas Mg cations predominantly have $\varepsilon_\parallel$. The strain magnitude increases with Mg fraction and significant local strain fluctuations occur. (b) Illustration of (Zn,Mg)O structures at 12.5% and 37.5% Mg fraction in addition to the corresponding strain ellipsoids centered around their respective cations. The inset includes an illustration of a strain ellipsoid, which represents the rigid rotation and elastic deformation of the local bonding environment around individual Zn and Mg cations at the atomic scale.

of (Zn,Mg)O configurations containing thousands of atoms, as detailed in Figs. S4 and S5 of the supplementary information (SI). This stochastic sampling approach simulates the microcanonical density of states as a function of the ensemble energy and provides accurate estimates for the configurational entropy assuming vibrational entropy to be negligible. The resulting free energies, along with representative structures, are shown in Figure 2.

By drawing common tangents between the free energies of formation as a function of composition at different temperatures [Figs. 2(a) and 2(b)], a phase diagram was constructed for the ZnO:MgO mixture [Figure 2(c)]. The predicted phase diagram is in close agreement with experimental data [37, 38, 39, 40, 41] and compares favorably with previous first-principles predictions [48, 49] using a single adjustable parameter (a uniform shift in the formation energies of the rocksalt configurations by 0.19 eV per formula unit, f.u.). On average, errors on relative formation energies are in the range of 0.2-0.8 eV per atom with a mean absolute deviation of 0.26 eV per atom [50]. This single-parameter correction is thus consistent with the typical error margins of density-functional-theory calculations.

To quantify Mg-induced distortions, the local strain around individual cations in each structure was calculated by examining the deformation from an ideal coordination environment of N nearest neighbors located at positions $\boldsymbol{R}_n$ to the corresponding distorted environment defined by the nearest-neighbor positions $\boldsymbol{r}_n$:

$$\boldsymbol{\varepsilon} = \frac{1}{2}\left(\boldsymbol{J}\boldsymbol{J}^\top - \boldsymbol{I}\right) = \frac{3}{2\bar{r}^2}\langle \boldsymbol{r}\boldsymbol{r}^\top \rangle - \frac{\boldsymbol{I}}{2}, \tag{1}$$

where $\langle \boldsymbol{r}\boldsymbol{r}^\top \rangle$ stands for $\frac{1}{N}\sum_{n=1}^{N} \boldsymbol{r}_n \boldsymbol{r}_n^\top$, $\boldsymbol{J}$ is the (best-fit) deformation matrix from $\boldsymbol{R}_n$ to $\boldsymbol{r}_n$, $\boldsymbol{I}$ is the

identity matrix, and $\bar{r}$ is the linear interpolation of the wurtzite O–Zn and O–Mg bond lengths. For simplicity, these local deformations are visualized as colored ellipsoids, whose shape represents the directional compression (in blue) or expansion (in red) of the Zn and Mg coordination environments in three dimensions (Figure 3) (cf. Figure S6, SI). In Figure 3(a), it is seen that Zn and Mg cations have distinct strain patterns. The strain surrounding Zn cations is a mixture of $\varepsilon_\perp$ and $\varepsilon_\parallel$, whereas that around Mg cations is predominantly of $\varepsilon_\parallel$ character. This phenomenon has previously been reported in similar cations in perovskite oxides [51]. As the Mg fraction increases, the magnitudes of $\varepsilon_\perp$ and $\varepsilon_\parallel$ increase, showing that Zn and Mg experience higher local strain in (Zn,Mg)O. Fluctuations of $\varepsilon_\perp$ and $\varepsilon_\parallel$ at intermediate concentrations are significantly larger than at dilute concentrations. These fluctuations can reach up to 1.5% in $\varepsilon_\perp$ and –2.5% in $\varepsilon_\parallel$, while the global strain (that is, their macroscopic average across the periodic supercell) never exceeds 1.0%. Visualizing the strain ellipsoids [Figure 3(b)] confirms that Mg cations exhibit significantly stronger uniaxial compression than Zn cations, whereas Zn cations exhibit marginally stronger biaxial tension than Mg cations. The central conclusion of this analysis is that cation ordering impacts local strain at the atomic scale by causing strong tetrahedral fluctuations from Mg onto neighboring Zn.

These fluctuations can be rationalized at the electronic-structure level by examining the oxygen–metal bonds and the hybridization of the oxygen and metal orbitals. (Representative atomic orbitals of Zn, Mg, and O are shown in Figure S7 of the SI.) As the Mg fraction increases, the average O–Zn bond length (basal-plane and polar, relative to the [0001] polar axis) increases [cf. Figure S8(a), SI], implying weakened bond strength. The onset of the smaller Mg cations induces larger O–Zn bond lengths. The weakening of the bonds was analyzed by calculating maximally localized Wannier functions [52, 53] in wurtzite ZnO and (Zn,Mg)O at 37.5% Mg to visualize and quantify O–Zn bonding interactions. A crystal orbital Hamilton population (COHP) [54] analysis was conducted to assess the strength of these interactions in (Zn,Mg)O (dashed) relative to ZnO (solid) [cf. Figure S8(b), SI]. Bonds in the basal plane are typically characterized by strong bonding peak intensities compared to polar bonds. Compared with bonding interactions in ZnO, the peak intensity of the basal-plane bonding in (Zn,Mg)O drops while the polar anti-bonding peak intensifies.

These results can be understood by considering bond ionicity [55]. The Zn–3d orbitals in ZnO participate in covalent bonding by partial electron donation while the Mg–3s orbitals fully donate their electrons to form ionic bonds. Upon substituting Zn for Mg in (Zn,Mg)O, fewer electrons from Zn–3d orbitals contribute to bonding, thereby distorting bonds across the tetrahedral network and inducing local strain fluctuations. Understanding the driving force of these fluctuations is critical to analyzing the pathways of ferroelectric switching in (Zn,Mg)O.

2.2 Influence of strain fluctuations on ferroelectricity

Nudged-elastic-band calculations [56, 57, 58] were conducted to determine the minimum energy pathways of ferroelectric polarization reversal in (Zn,Mg)O. The spontaneous polarization of each image along the pathways was calculated (cf. Figure S9, SI). Minimum energy pathways at 0% Mg and 37.5% Mg are shown in Figure 4(a). In the case of 0% Mg (pure ZnO), there exist little to no strain fluctuations, leading to uniform switching where all atoms switch simultaneously in one step. At 37.5% Mg, there exist significant local strain fluctuations such that the structure engages in sequential switching where cations move consecutively in multiple steps, a phenomenon previously reported in corundum derivatives [59]. These types of reversal mechanisms are also characterized by intermediate states passing through a non-polar h-BN crystal structure for uniform reversal and an anti-polar crystal structure with alternating polar states for sequential reversal. This reversal mechanism has been recently observed experimentally and computationally in a related wurtzite

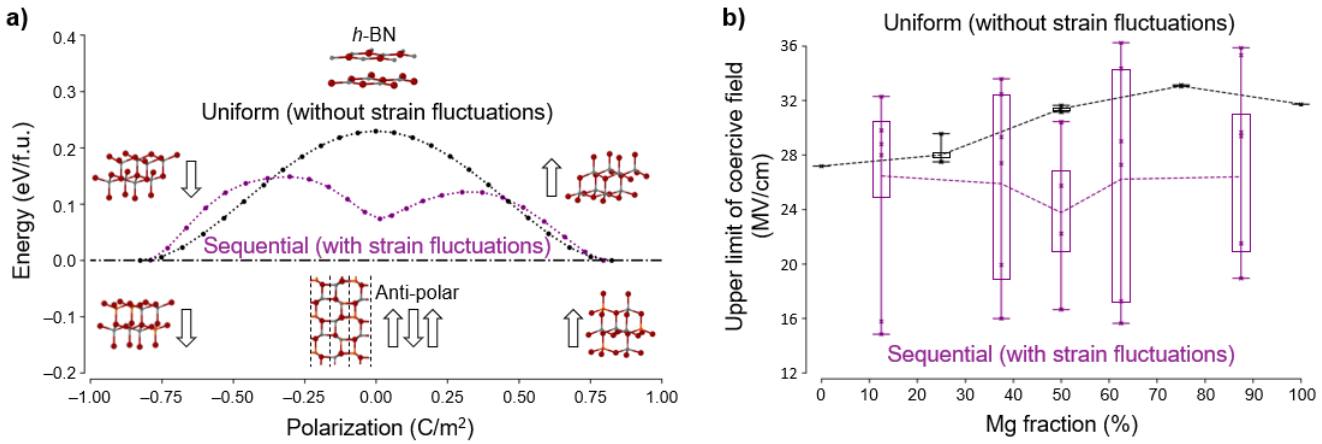

Figure 4: (a) Minimum energy pathways of (Zn,Mg)O simulated using nudged-elastic-band calculations. Here, Mg fractions of 0% and 37.5% are shown to illustrate the effect of strain fluctuations on the ferroelectric polarization reversal. While uniform reversal (black) passes through a hexagonal boron nitride (h-BN) intermediate structure, sequential reversal (purple) passes through an anti-polar structure with alternating polar states. Sequential reversal reduces the energy barrier between the bistable states by 40%. (b) Estimates of the coercive field and its variance under uniform and sequential reversal. If a structure contains larger strain fluctuations, there is a strong likelihood that it will undergo a sequential ferroelectric reversal under reduced coercive fields. Unless the minimum energy pathway is the actual pathway, these calculations of the coercive fields are an upper limit of the experimental coercive field.

material, (Al,B)N [29]. Sequential reversal leads to a 40% reduction in the energy barrier compared to uniform reversal. This reduction in the reversal barrier is further validated when considering the estimated coercive field [Figure 4(b)]. Uniform reversal with little strain fluctuations leads to high coercive fields with little variance in the electric field, whereas sequential reversal with significant fluctuations is characterized not just by lower coercive fields, but also by a larger variance of these fields, with a reduction of at least 45%. Unless the minimum energy pathway is the actual pathway, these calculations of the coercive fields are an upper limit of the experimental coercive field. With these large spreads, there are opportunities for the most favorably distorted cation to switch first, prompting nearby cations to switch consecutively.

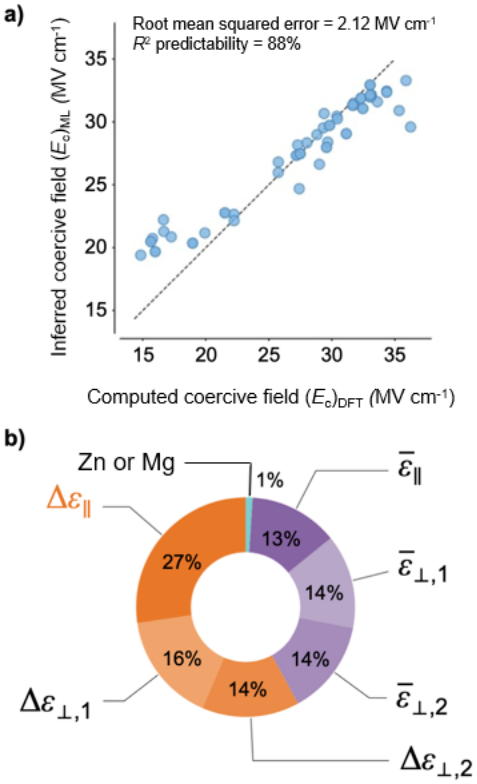

Figure 5: Ensemble-learning nonlinear regression of local coercive fields. (a) Comparison of the computed and predicted reversal barriers from the multivariate regression model. The regression model predicts local coercive fields with a root mean square error of 2.12 MV cm^{-1} and a coefficient of determination of 88%. (b) Feature importance ranking of the regression model including changes in strain between the bistable states ($\Delta\varepsilon$) (in orange) and mean strains ($\bar{\varepsilon}$) (in purple). The most important features are changes in the uniaxial ($\Delta\varepsilon_{\parallel}$) and biaxial strain ($\Delta\varepsilon_{\perp}$). The least important feature of the model was the atom type (*e.g.*, Zn or Mg).

To confirm the prevalence of strain fluctuations in inducing ferroelectricity in (Zn,Mg)O, a multivariate nonlinear regression model [60, 61] was applied to the local coercive fields. In this model, the local strains in the negatively and positively poled states of each cation were parsed to obtain a database of strain- and cation-dependent input features, namely, the strain in the initial and final poled states ($\varepsilon_{\parallel}^{+}$, $\varepsilon_{\perp}^{+}$, $\varepsilon_{\parallel}^{-}$, and $\varepsilon_{\perp}^{-}$), the changes in strain between the bistable states ($\Delta\varepsilon_{\parallel} = \varepsilon_{\parallel}^{+} - \varepsilon_{\parallel}^{-}$ and $\Delta\varepsilon_{\perp} = \varepsilon_{\perp}^{+} - \varepsilon_{\perp}^{-}$), the mean strains [$\bar{\varepsilon}_{\parallel} = (\varepsilon_{\parallel}^{+} + \varepsilon_{\parallel}^{-})/2$ and $\bar{\varepsilon}_{\perp} = (\varepsilon_{\perp}^{+} + \varepsilon_{\perp}^{-})/2$], and the identity of the switching cation (Zn or Mg). The local coercive field (the output) was calculated by applying a multi-Gaussian fitting on the nudged-elastic-band pathways. Training and validation of the regression model are provided in Figure 5(a), resulting in a root mean square error (RMSE) of 2.12 MV cm^{-1} and a high coefficient of determination (R^2) of 88%. Discrepancies between simulations and the regression model are limited to the lowest and highest coercive fields, suggesting that second-nearest-neighbor strain fluctuations may influence local coercive fields to some extent.

Feature importance ranking reveals that the dominant contributors to the coercive field are the changes in the uniaxial compression $-\Delta\varepsilon_{\parallel}$ and biaxial tension $\Delta\varepsilon_{\perp}$ between the poled states [Figure 5(b)]. As illustrated in the partial dependency plots (Figure S12, SI) [61, 62, 63], the coercive field is minimized when $\Delta\varepsilon_{\parallel}$ is in the range of -1.2 to -0.4% and $\Delta\varepsilon_{\perp}$ is below 0%. The

regression model also reveals that the identity of the cation (Zn or Mg) has little bearing on the coercive field. To critically assess this observation, the minimum energy pathway of chemically pristine, locally strained ZnO was calculated at the nanoscale and mesoscale (Figure S13, SI), in addition to hysteresis measurements of heterostructures containing (Zn,Mg)O and ZnO thin films (Figure S14, SI). The calculation and experiment demonstrate that strain fluctuation is in itself a sufficient driving force for sequential switching under reduced coercive fields in ZnO. In other words, although chemical substitution is one possible vehicle for strain fluctuations to occur, it does not directly determine the local coercive fields. This result offers conclusive evidence that longitudinal strain fluctuations ($\Delta\varepsilon_{\parallel}$) can effectively promote ferroelectricity in wurtzites.

3 Conclusion

This work has shown that (Zn,Mg)O exhibits local strains that largely exceed their macroscopic average. The computed ZnO:MgO phase diagram was found to be consistent with experimental data using a single corrective parameter, enabling the modeling of representative local configurations in (Zn,Mg)O. Using the predicted configurations, this study unveiled the atomistic mechanisms of ferroelectric switching in this material, demonstrating that Mg cations disrupt chemical bonding along the tetrahedral network; these bond disruptions induce atomic-scale strain fluctuations, which trigger ferroelectricity *via* sequential polarization reversal. If cation ordering in (Zn,Mg)O were to be controlled to maximize strain fluctuation along the polar axis (by, *e.g.*, synthesizing ZnO/MgO heterostructures or introducing Zn/Mg composition gradients along the polar direction), one could optimize sequential polarization switching. This approach provides an effective and broadly applicable design principle to unlock ferroelectricity in wurtzites and related families of polar materials.

4 Acknowledgements

Funding: The calculations and experiments were supported by the U.S. Department of Energy, Office of Science, Office of Basic Energy Sciences Energy Frontier Research Centers program under Award Number DE-SC0021118 (Center for 3D Ferroelectric Microelectronics). All first-principles calculations and analyses were conducted using the Pennsylvania State University ROAR supercomputer resources of the Institute for Computational and Data Sciences.

Author contributions: *conceptualization*–S. M. B., S. E. T.-M., A. C. T. V., J.-P. M., A. M. R., I. D.; *methodology*–S. M. B., S. G., S. O., R. J. S., A. S., L. J.; *software*–S. M. B., S. G., S. O., A. S., A. C. T. V., I. D.; *formal analysis*–S. M. B., S. O., R. J. S., A. S., L. J.; *data curation*–S. M. B; *review and editing*–all authors; *visualization*–S. M. B, S. O., I. D.; *project administration*–S. E. T.-M.; *funding acquisition*–S. E T.-M.; I. D.

Conflicts of interest: The authors declare no conflicts of interest.

Data and materials availability: The data that support the findings of this study are available from the corresponding author upon reasonable request.

References

[1] Dawber, M., Rabe, K. M. & Scott, J. F. *Rev. Mod. Phys.* **77**, 1083 (2005).

[2] Mikolajick, T., Schroeder, U. & Slesazeck, S. *IEEE Trans. Electron Devices* **67**, 1434–1443 (2020).

[3] Cohen, R. E. *Nature* **358**, 136–138 (1992).

[4] Xu, P. *et al. J. Chem. Inf. Model.* **62**, 5038–5049 (2022).

[5] Izyumskaya, N. *et al. Crit. Rev. Solid State Mater. Sci.* **32**, 111–202 (2007).

[6] Morrison, F. D., Jung, D. J. & Scott, J. F. *J. Appl. Phys.* **101**, 094112 (2007).

[7] Ma, T. & Han, J.-P. *IEEE Electron Device Lett.* **23**, 386–388 (2002).

[8] Kohlstedt, H. *et al. Microelectron. Eng.* **80**, 296–304 (2005).

[9] Kim, Y. S. *et al. Appl. Phys. Lett.* **86**, 102907 (2005).

[10] Nagarajan, V. *et al. Appl. Phys. Lett.* **86**, 192910 (2005).

[11] Ihlefeld, J. F. *et al. J. Am. Ceram. Soc.* **99**, 2537–2557 (2016).

[12] Park, J. Y. *et al. J. Appl. Phys.* **128**, 240904 (2020).

[13] Park, J. Y. *et al. Adv. Mater.* 2204904 (2022).

[14] Kim, K.-H., Karpov, I., Olsson, R. H. & Jariwala, D. *Nat. Nanotechnol.* **18**, 422–441 (2023).

[15] Park, M. H., Lee, Y. H., Mikolajick, T., Schroeder, U. & Hwang, C. S. *MRS Commun.* **8**, 795–808 (2018).

[16] Song, T. *et al. ACS Appl. Electron. Mater.* **3**, 4809–4816 (2021).

[17] Schroeder, U. *et al. Inorg. Chem.* **57**, 2752–2765 (2018).

[18] Mueller, S. *et al. ECS J. Solid State Sci. Technol.* **1**, N123 (2012).

[19] Mohan, J. *et al. ACS Appl. Electron. Mater.* **4**, 1405–1414 (2022).

[20] Jung, Y. C. *et al. Appl. Phys. Lett.* **121**, 222901 (2022).

[21] Zhou, S., Zhang, J. & Rappe, A. M. *Sci. Adv.* **8** (2022).

[22] Lomenzo, P. D., Richter, C., Mikolajick, T. & Schroeder, U. *ACS Appl. Electron. Mater.* **2**, 1583–1595 (2020).

[23] Skopkin, E., Guillaume, N., Alrifai, L., Gonon, P. & Bsiesy, A. *Appl. Phys. Lett.* **120**, 172901 (2022).

[24] Cheema, S. S. *et al. Nature* **604**, 65–71 (2022).

[25] Yu, Z. *et al. ACS Appl. Mater. Interfaces* **14**, 53057–53064 (2022).

[26] Konishi, A. *et al. Appl. Phys. Lett.* **109**, 102903 (2016).

[27] Moriwake, H. *et al. Appl. Phys. Lett.* **104**, 242909 (2014).

[28] Moriwake, H. *et al. APL Mater.* **8**, 121102 (2020).

[29] Calderon, S. *et al. Science* **380**, 1034–1038 (2023).

[30] Shimizu, T. *et al. Sci. Rep.* **6**, 32931 (2016).

[31] Yazawa, K., Drury, D., Zakutayev, A. & Brennecka, G. L. *Appl. Phys. Lett.* **118**, 162903 (2021).

[32] Yazawa, K., Mangum, J. S., Gorai, P., Brennecka, G. L. & Zakutayev, A. *J. Mater. Chem. C* **10**, 17557–17566 (2022).

[33] Drury, D. *et al. Phys. Status Solidi RRL* **15**, 2100043 (2021).

[34] Wolff, N. *et al. J. Appl. Phys.* **129**, 034103 (2021).

[35] Ferri, K. *et al. J. Appl. Phys.* **130**, 044101 (2021).

[36] Sarasamak, K., Kulkarni, A. J., Zhou, M. & Limpijumnong, S. *Phys. Rev. B* **77**, 024104 (2008).

[37] Xia, L., Liu, Z. & Taskinen, P. *J. Alloys Compd.* **687**, 827–832 (2016).

[38] Sarver, J. F., Katnack, F. L. & Hummel, F. A. *J. Electrochem. Soc.* **106**, 960–963 (1959).

[39] Segnit, E. R. & Holland, A. E. *J. Am. Ceram. Soc.* **48**, 409–413 (1965).

[40] Raghavan, S., Hajra, J., Iyengar, G. N. K. & Abraham, K. P. *Thermochim. Acta* **189**, 151–158 (1991).

[41] Kenny, D. S. & Navrotsky, A. *J. Inorg. Nucl. Chem.* **34**, 2115–2119 (1972).

[42] Ångqvist, M. *et al. Adv. Theory Simul.* **2**, 1900015 (2019).

[43] Sanchez, J. M., Ducastelle, F. & Gratias, D. *Phys. A: Stat. Mech.* **128**, 334–350 (1984).

[44] van de Walle, A. *CALPHAD: Comput. Coupling Ph. Diagr. Thermochem.* **33**, 266–278 (2009).

[45] Wang, F. & Landau, D. P. *Phys. Rev. Lett.* **86**, 2050 (2001).

[46] Wang, F. & Landau, D. P. *Phys. Rev. E* **64**, 056101 (2001).

[47] Landau, D. P., Tsai, S.-H. & Exler, M. *Am. J. Phys.* **72**, 1294 (2004).

[48] Liu, B., Seko, A. & Tanaka, I. *Phys. Rev. B* **86**, 245202 (2012).

[49] Koster, R. S., Fang, C. M., Dijkstra, M., van Blaaderen, A. & van Huis, M. A. *J. Phys. Chem. C* **119**, 5648–5656 (2015).

[50] Stevanović, V. & Lany, S. *Phys. Rev. B* **85**, 115104 (2012).

[51] Grinberg, I., Suchomel, M. R., Davies, P. K. & Rappe, A. M. *J. Appl. Phys.* **98**, 094111 (2005).

[52] Marzari, N., Mostofi, A., Yates, J., Souza, I. & Vanderbilt, D. *Rev. Mod. Phys.* **84**, 1419 (2012).

[53] Pizzi, G. *et al. J. Phys.: Condens. Matter* **32**, 165902 (2020).

[54] Dronskowski, R. & Bloechl, P. E. *J. Phys. Chem.* **97**, 8617–8624 (1993).

[55] Grinberg, I. *et al. Phys. Rev. Lett* **98**, 107601 (2007).

[56] Jónsson, H., Mills, G. & Jacobsen, K. W. *Classical and Quantum Dynamics in Condensed Phase Systems* (World Scientific, 1998).

[57] Henkelman, G. & Jónsson, H. *J. Chem. Phys.* **113**, 9978 (2000).

[58] Henkelman, G., Uberuaga, B. P. & Jónsson, H. *J. Chem. Phys.* **113**, 9901 (2000).

[59] Ye, M. & Vanderbilt, D. *Phys. Rev. B* **93**, 134303 (2016).

[60] Breiman, L. *Mach. Learn.* **45**, 5–32 (2001).

[61] Molnar, C. *Interpretable Machine Learning: A Guide for Making Black Box Models Explainable* (Lulu. com, 2020).

[62] Friedman, J. H. *Ann. Statist.* **29**, 1189–1232 (2001).

[63] Zhao, Q. & Hastie, T. *J. Bus. Econ. Stat.* **39**, 272–281 (2019).